An Ionized Outflow in Orion-KL Source I?

Melvyn Wright[1], Tomoya Hirota[2], Jan Forbrich[3], Richard Plambeck[4], John Bally[5], Ciriaco Goddi[6,7,8,9],
Adam Ginsburg[10], and Brett McGuire[11,12]

[1] Department of Astronomy, University of California, Berkeley, 501 Campbell Hall, Berkeley, CA 94720-3441, USA; melvyn@berkeley.edu
[2] Mizusawa VLBI Observatory, National Astronomical Observatory of Japan, 2-12, Hoshigaoka, Mizusawa, Oshu, Iwate 023-0861, Japan
[3] Centre for Astrophysics Research, University of Hertfordshire, College Lane, Hatfield, AL10 9AB, UK
[4] Radio Astronomy Lab, University of California, Berkeley, 501 Campbell Hall, Berkeley, CA 94720-3441, USA
[5] CASA, University of Colorado, 389-UCB, Boulder, CO 80309, USA
[6] Instituto de Astronomia, Geofísica e Ciências Atmosféricas, Departamento de Astronomia, Universidade de São Paulo, São Paulo, SP 05508-090, Brazil
[7] Dipartimento di Fisica, Università degli Studi di Cagliari, SP Monserrato-Sestu km 0.7, I-09042 Monserrato, Italy
[8] INAF—Osservatorio Astronomico di Cagliari, via della Scienza 5, I-09047 Selargius (CA), Italy
[9] INFN, Sezione di Cagliari, Cittadella Univ., I-09042 Monserrato (CA), Italy
[10] Department of Astronomy, University of Florida, 211 Bryant Space Science Center, P.O Box 112055, Gainesville, FL 32611-2055 USA
[11] Department of Chemistry, Massachusetts Institute of Technology, Cambridge, MA 02139, USA
[12] National Radio Astronomy Observatory, Charlottesville, VA 22903, USA

Abstract

We present images at 6 and 14 GHz of Source I (SrcI) in the Kleinmann–Low Nebula in Orion. At higher frequencies, from 43 to 340 GHz, images of this source are dominated by thermal emission from dust in a 100 au diameter circumstellar disk, but at 6 and 14 GHz the emission is elongated along the minor axis of the disk, aligned with the SiO bipolar outflow from the central object. Gaussian fits to the 6, 14, 43, and 99 GHz images find a component along the disk minor axis whose flux and length vary with frequency consistent with free–free emission from an ionized outflow. The data favor a broad outflow from a disk wind, rather than a narrow ionized jet. SrcI was undetected in higher-resolution 5 GHz e-MERLIN observations obtained in 2021. The 5–6 GHz structure of SrcI may be resolved out by the high sidelobe structure of the e-MERLIN synthesized beam, or be time variable.

Unified Astronomy Thesaurus concepts: Radio continuum emission (1340)

1. Introduction

Jets and outflows are closely associated with accretion in the formation of stars. Free–free (thermal) radio continuum emission is associated with these jets. The emission is weak and compact, and high angular resolution at centimeter wavelengths is required to map this emission because of high opacity at millimeter and IR wavelengths; see, e.g., the review by Anglada et al. (2018). Protostellar outflows transfer momentum and kinetic energy to outer envelopes and influence future star formation in surrounding regions. Outflows extract excess angular momenta from protostars and their surrounding disks to enable mass accretion. The mechanisms to drive outflows, such as entrainment of molecular gas by a higher-velocity jet or an MHD-driven outflow by magneto-centrifugal disk winds, are still poorly understood. Commerćon et al. (2022) studied the evolution of disks, accretion and outflow in massive stars using high-resolution numerical simulations with several different numerical codes. Outflows may be driven by both radiation pressure and MHD mechanisms. The properties of the accretion disk around massive protostars depends on the physics, including hydrodynamics, magnetic fields, and ambipolar diffusion. In this paper we present new observations of the outflow and accretion disk in the massive young protostar, Source I (SrcI), and discuss the possible emission mechanisms which may help to constrain the theoretical models of massive star formation.

The Kleinmann–Low Nebula (KL) in Orion, at a distance of 415 pc (Menten et al. 2007; Kim et al. 2008; Kounkel et al. 2018), is the nearest H II region in which massive ($M > 8\ M_\odot$) stars are forming. The two most massive objects in this region, SrcI and the Becklin–Neugebauer Object (BN), appear to be recoiling from one another at 35–40 km s^{-1} (Rodríguez et al. 2005; Gómez et al. 2008; Goddi et al. 2011b), suggesting that they were ejected from a multiple system via dynamical decay approximately 550 yr ago (Rodríguez et al. 2017, 2020; Bally et al. 2020). SrcI has an estimated mass of $\sim15\ M_\odot$ (Ginsburg et al. 2018), with a rotating accretion disk, a hot inner core obscured by a dusty outer envelope, and a young molecular outflow that is prominent in shock-tracing SiO in several rotational-vibration levels extending out along the minor axis of the disk.

The region around SrcI has been well studied since the 1980s (Hirota et al. 2014; Plambeck & Wright 2016); it is an active source associated with variable SiO and H$_2$O masers (Reid et al. 2007; Goddi et al. 2009, 2011b; Plambeck et al. 2009; Matthews et al. 2010; Niederhofer et al. 2012; Greenhill et al. 2013). Ginsburg et al. (2018) fitted the observed structure of the disk using 90 and 230 GHz Atacama Large Millimeter/submillimeter Array (ALMA) continuum observations at 50 and 20 mas resolution. They determined that the disk has a length of ~100 au and vertical FWHM height of ~20 au. The disk major axis increases with observing frequency from 43 to 340 GHz, which is expected as the dust optical depth increases. Images of the spectral index distributions from 43 to 340 GHz show an extensive region with spectral index <2 along the minor axis of the disk. Although the high opacity at 220–340 GHz hides the internal structure of the disk, images at 43–99 GHz reveal structure within the disk (Wright et al. 2022).

Table 1
Observations

Freq (GHz)	Project Code	Date	Time (min)	Synth Beam (milliarcsec)	Baseline (meters)
5	e-MERLIN/CY12202	2021-10-23,25,26	1023	120×30 at PA 20	2400–217,500
6	VLA/SD630	2012-9-30	291	300×194 at PA 30	500–36,600
14	VLA22A-022	2022-6-4	200	280×160 at PA 42	500–36,600
43	VLA/AC952	2009-1-12	198	58×39 at PA 3	500–36,600
43	VLA/18A-136	2018-3-6	291	39×34 at PA 1	500–36,600
86 and 99	2017.1.00497.S	2017-10-12	158	45×36 at PA 47	40-16,200
224	2016.1.00165.S	2017-9-19	44	39×19 at PA 66	40–10,500
340	2016.1.00165.S	2017-11-8	45	26×11 at PA 58	90–12,900

At lower frequencies, the spectral energy distribution (SED) suggests that free–free emission may become important. Plambeck & Wright (2016) analyzed the continuum flux densities measured for SrcI from 4 to 690 GHz. Free–free emission may become important where the dust emission becomes optically thin.

In this paper, we present 6 and 14 GHz images of the emission of the SrcI disk in Orion-KL with $\sim 0\rlap{.}''3 \times 0\rlap{.}''2$ resolution, and observations with the e-MERLIN telescope at 5 GHz with a synthesized beam FWHM 120×30 mas. We analyze the continuum images from 6 to 99 GHz to trace the structure along the minor axis of the SrcI disk. The 6 and 14 GHz emission extends out along the minor axis of the disk, and may be evidence for a dusty ionized outflow from SrcI.

This paper is organized as follows. Section 2 presents the observations and data reduction, Section 3 discusses the results for the SrcI disk and outflow, and discusses different emission mechanisms, and Section 4 summarizes the conclusions.

2. Observations and Data Reduction

We used JVLA[13] and ALMA data at 6, 14, 43, 86, 99, 223, and 340 GHz to image the continuum emission from SrcI. Table 1 provides a summary of the observations, including project codes and synthesized beam FWHMs obtained with a robust $= -2$ weighting of the uv data. The MIRIAD software package (Sault et al. 1995) was used to analyze the data in this paper.

The 43 GHz and 99 GHz (ALMA Band 3; B3) observations and calibration are described in Hirota et al. (2020) and Wright et al. (2020). The 86 GHz observations are described in Wright et al. (2022). The 223 GHz (ALMA Band 6; B6) and 340 GHz (ALMA Band 7; B7) observations and calibration are described in Ginsburg et al. (2018).

We present a continuum image at 6 GHz using the data described in Forbrich et al. (2016). Figure 1 shows the image of SrcI using uv data $>100 k\lambda$ to filter out large-scale structure from Orion. Observations at 14 GHz were obtained using the JVLA on 2022 June 4. These observations were calibrated using observatory-provided scripts. Synthesized images were made using the CASA task tclean. The synthesised beam FWHM was 280×160 mas with a position angle (PA) of $42°$ using a robust $= 2$ weighting of the uv data. Figure 1 shows the resulting image of SrcI.

Observations with the e-MERLIN array were obtained on 2021 October 23, 25, and 26 (epoch 2021.81) at 5 GHz. Six antennas among seven e-MERLIN stations (except Darnhall)

---

were used; the Lovell telescope participated only on October 23. Baseline lengths ranged from 40 to 3850 $k\lambda$ with a uv hole of 200 k–400 $k\lambda$. A standard spectral setting was employed, in which the four spectral windows with 128 MHz bandwidth and 1 MHz resolution were assigned with center frequencies at 4.880 GHz, 5.008 GHz, 5.135 GHz, and 5.264 GHz. These observations were calibrated using observatory-provided scripts of CASA. Self-calibration and imaging were done using CASA. A Briggs weighting with a robustness parameter of 0.5 was employed. In order to exclude contributions from extended emission (see Section 3.3), we use visibility data only with longer baseline lengths than 200 $k\lambda$. The synthesized beam was 120×30 mas with a PA of $20°$. The pixel size and the field of view were 15 mas and $4'$, respectively. The rms noise level of the self-calibrated image was 30 μJy, while the noise levels were significantly higher around strong point sources due to their sidelobes. SrcI was not detected in this image.

3. Discussion

3.1. Disk Structure

Ginsburg et al. (2018) fitted the observed structure of the disk from B3 and B6 ALMA continuum observations at 50 and 20 mas resolution, respectively. They determined that the disk has a length of ~ 100 au and vertical FWHM height of ~ 20 au. The integrated flux density for SrcI from 43 to 340 GHz has a spectral index of ~ 2, consistent with optically thick dust emission (Plambeck & Wright 2016). However, images of the spectral index across the source reveal an extensive region with spectral index < 2 along the minor axis of the disk (Wright et al. 2020, 2022). Although the high opacity at 220–340 GHz hides the internal structure of the disk, images at 43 to 99 GHz reveal structure within the disk (Wright et al. 2022).

Table 2 summarizes the results of Gaussian fits to SrcI for the 6–340 GHz images. The disk major axis, at PA $\sim -38°$, increases with observing frequency from 43 to 340 GHz, which is expected as the dust optical depth increases. At 6 and 14 GHz, however, the emission is extended at PA $\sim 55°$, along the disk's minor axis. The major axis of SrcI at centimeter wavelengths is nearly perpendicular to the major axis at millimeter wavelengths. This is also evident in Rodríguez et al. (2017; see their Table 2). The 6 and 14 GHz Gaussian fits are overlaid on a 99 GHz image in Figure 1. Since the observations were obtained at different epochs (Table 1) we must correct the positions for the proper motion of SrcI, moving at $Dx = 6.3$, $Dy = -4.2$ mas yr^{-1} (Goddi et al. 2011a). We adjusted the 6 GHz and 14 GHz images of SrcI for proper motion to the 99 GHz epoch. After this correction, the 6 GHz peak coincides
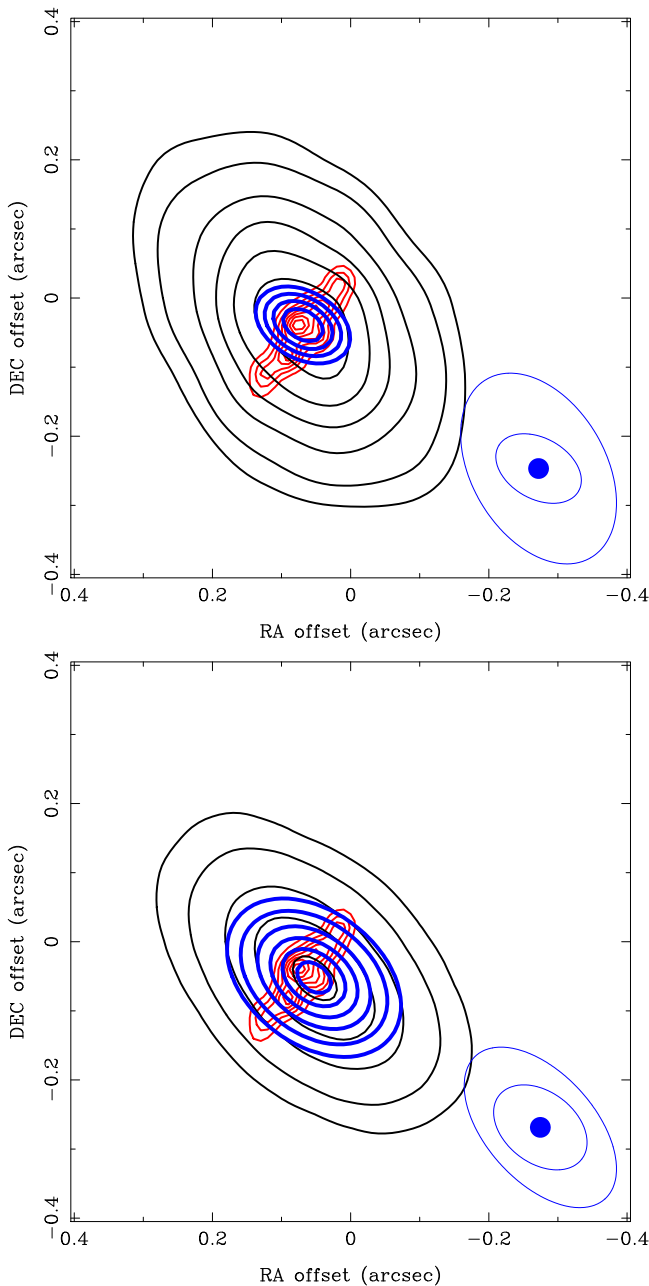
Figure 1. Top: Source I (SrcI) continuum emission at 6 GHz (black), and Gaussian model (blue). Contour levels: 0.05, 0.1, 0.2, 0.3, 0.4, 0.5, and 0.6 mJy beam^{-1}, superposed on the 99 GHz model showing the disk emission at 30 mas resolution (red). Contour levels 1, 2, 3, 4, 5, 6, 7 mJy beam^{-1}. The synthesized beam and the Gaussian model at 6 GHz, and the 99 GHz model FWHM are shown as ellipses in the lower right. Bottom: SrcI continuum emission at 14 GHz (black), and Gaussian model (blue). Contour levels: 0.2, 0.4, 0.8, 1.2, 1.6, and 2 mJy beam^{-1}, superposed on the 99 GHz model showing the disk emission at 30 mas resolution (red). Contour levels 1, 2, 3, 4, 5, 6, 7 mJy beam^{-1}. The synthesized beam and the Gaussian model at 14 GHz and the 99 GHz model FWHM are shown as ellipses in the lower right.

with the center of the disk at 43 and 99 GHz within 5 mas, but the 14 GHz peak is offset to the southwest by ∼70 mas. The absolute position accuracy is estimated to be 20–30 mas (see the discussion in Forbrich et al. 2016 and in the Very Large Array (VLA) manuals[14]), so this positional discrepancy

suggests the possible presence of unresolved asymmetric structures that are not well fitted by a single Gaussian, or of time variability in the emission.

Weak emission extending along the minor axis of the disk is also apparent at 43 and 99 GHz. We used two-component Gaussian fits to estimate the flux and length of this structure, using the single Gaussian fit at 99 GHz along the disk major axis and the Gaussian fit at 6 GHz along the minor axis as initial parameters for the fits. Figures 2 and 3 show the 43 and 99 GHz continuum images and model fits. The parameters for the two-Gaussian fits are included in Table 2. The Gaussian components along the disk major axis are consistent with the single Gaussian fits. The second Gaussian component is aligned with the disk minor axis, but the flux and length vary with frequency, and are plotted in Figure 5. Note that the component along the disk minor axis is ∼23% of the total flux at 43 GHz, and only ∼7% at 99 GHz.

We also fitted the lower signal-to-noise 86 GHz continuum image, obtained with smaller continuum bandwidth (Wright et al. 2022), with two Gaussian components. The Gaussian component along the disk major axis is consistent with the single Gaussian fit. The flux of the second Gaussian component is consistent with the 99 GHz result, but the PA and size of this component depend strongly on the choice of image resolution fitted and have large estimated errors, and hence are omitted from Table 2 and Figure 5.

The 43 GHz images of SrcI in Goddi et al. (2011a) also suggest that there is a component along the minor axis of the disk. Their Figure 2 shows four 43 GHz continuum images of SrcI observed with the JVLA in the A configuration between 2000 November and 2009 January. There appears to be no significant change in the morphology or PA of the structure over 8 yr. The morphology is difficult to constrain in these data with different resolutions and sensitivity, but the flux could have changed by up to 20%, and a 10% change in structure is possible. We fitted a two-component Gaussian model to the highest signal-to-noise image (AC952, 2009 January 12; Table 1). A robust fit was obtained, consistent with the current 43 GHz image with a second Gaussian component along the disk minor axis with fitted parameters within 10%.

3.1.1. Compact Hot Spot

This section discusses the small-scale structure in the SrcI disk. The Gaussian models in Table 2 are robust fits to the overall structure of SrcI, but do not preclude more complex small-scale structure. The high-resolution 43 GHz observations of Reid et al. (2007) resolved SrcI into a disk plus a compact, 2.2 mJy source at 34 mas resolution (Reid et al. 2007, their Figure 1). Reid et al. (2007) also note that the disk appears to be warped with a component in PA 45° along the minor axis of the disk, which could indicate that there is a weak jet perpendicular to the disk. Wright et al. (2022) in their Figure 4, show the warped ridge structure in the 43, 86, and 99 GHz images at 30 mas resolution. At 99 GHz there is an unresolved component with a position R.A.: 05:35:14.518, decl.: −05:22:30.608 and a peak brightness 4.4 ± 0.2 mJy beam^{-1} at 30 mas resolution. The 43 GHz residuals to a two-Gaussian fit (Figure 2) reveal complex small-scale structure with peak residuals ±5σ. Fitting a point source to the peak residual at 43 GHz gives a flux density 0.13 ± 0.05 mJy in a 60 × 40 mas beam, at R.A.: 05:35:14.519, decl.: −05:22:30.611, which agrees with the 99 GHz position within a few milliarcsecond.
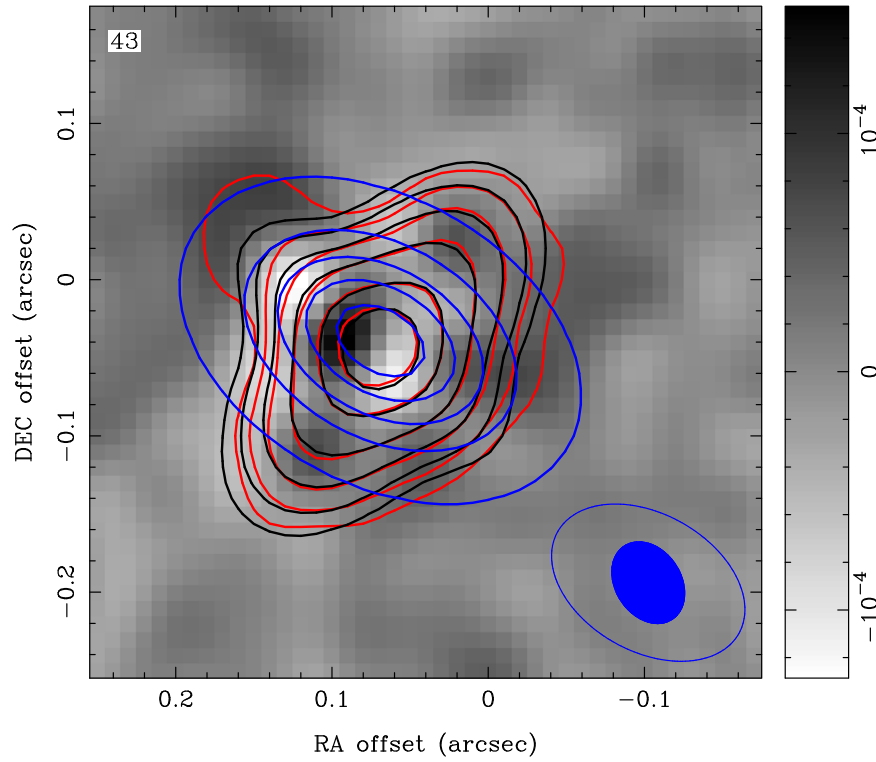
Figure 2. 43 GHz continuum emission and residuals to a two-Gaussian model fit. The red contours show the 43 GHz continuum emission convolved to 56×42 mas FWHM resolution. The black contours show the two-Gaussian model, both with contours at 25, 50, 100, 200, 400, 600, 800, and 1000 K . The pixel image shows residuals to the two-Gaussian model fit (units of jansky per beam). The blue contours show the single Gaussian fit to the 6 GHz continuum emission. Contours at 100, 500, 900, 1300, and 1700 K. The 43 GHz synthesized beam FWHM is indicated by the blue filled ellipse in the lower right. The 6 GHz Gaussian fitted FWHM is indicated by the blue open ellipse in the lower right.

Table 2
Measured Sizes and Flux Densities for Source I

Freq (GHz)	Gaussian Components	Deconvolved Size (arcsec)	PA (deg)	Integrated Flux (mJy)
6	1	$0.133 \pm 0.01 \times 0.088 \pm 0.010$	$61° \pm 3°$	$0.7 \pm .1$
14	1	$0.151 \pm 0.01 \times 0.103 \pm 0.010$	$53° \pm 4°$	$2.2 \pm .2$
43	1	$0.099 \pm 0.002 \times 0.057 \pm 0.002$	$-40°.4 \pm 3°$	10 ± 1
43	2	$0.125 \pm 0.002 \times 0.044 \pm 0.002$	$-39°.4 \pm 1°$	7.6 ± 1
43	2	$0.097 \pm 0.002 \times 0.030 \pm 0.002$	$53° \pm 3°$	2.3 ± 0.5
86	1	$0.142 \pm 0.005 \times 0.044 \pm 0.001$	$-38°.0 \pm 1°.0$	48 ± 5
99	1	$0.151 \pm 0.005 \times 0.044 \pm 0.002$	$-37°.8 \pm 1°.3$	58 ± 6
99	2	$0.163 \pm 0.005 \times 0.041 \pm 0.002$	$-37°.8 \pm 1°.0$	55 ± 6
99	2	$0.081 \pm 0.005 \times 0.029 \pm 0.002$	$56° \pm 3°$	4 ± 1
224	1	$0.197 \pm 0.003 \times 0.042 \pm 0.003$	$-37°.3 \pm 0°.4$	256 ± 25
340	1	$0.234 \pm 0.005 \times 0.042 \pm 0.002$	$-37°.4 \pm 0°.3$	630 ± 63

We note that our 43 GHz observations were self-calibrated using SiO masers, and then aligned with the 99 GHz image using the MIRIAD task IMDIFF, which finds optimum parameters in a maximum-likelihood sense, to minimize the difference between 43 and 99 GHz images, so we are actually measuring the position of the peak relative to the overall structure of the disk at 43 GHz. Ginsburg et al. (2018) detected a compact source at 224 and 93 GHz with flux ∼15 and 5.7 mJy, respectively (Ginsburg et al. 2018, their Table 4). The spectral index (SI) from 224 to 93 GHz is ∼1.1. Including the 43 GHz point-source fit at similar resolution (Reid et al. 2007), the SI from 224 to 43 GHz is ∼1.2. The compact source could be evidence for a compact outflow from one of the binary protostars, or a merger remnant. The source is offset from the

center of the disk, and appears to be extended along the disk major axis at 224 GHz. As discussed by Ginsburg et al. (2018), it is likely that the source is thermal but is more attenuated by the disk at 224 GHz than 93 and 43 GHz. If SrcI's central source is a binary, the offset from the disk midpoint may indicate the proximity of one of the protostars close to the inner edge of a circumbinary accretion disk. This suggests a binary orbit ∼5 au. The orbital time is only ∼3 yr. It will be interesting to see if the hot spot is variable on such a timescale.

Higher-resolution observations are required to see if the minor-axis emission at 43 and 99 GHz is associated with the compact hot spot in the disk, rather than being centered on the circumbinary disk. More compact Gaussian or point-source fits to the 6 and 14 GHz images have higher residuals; these
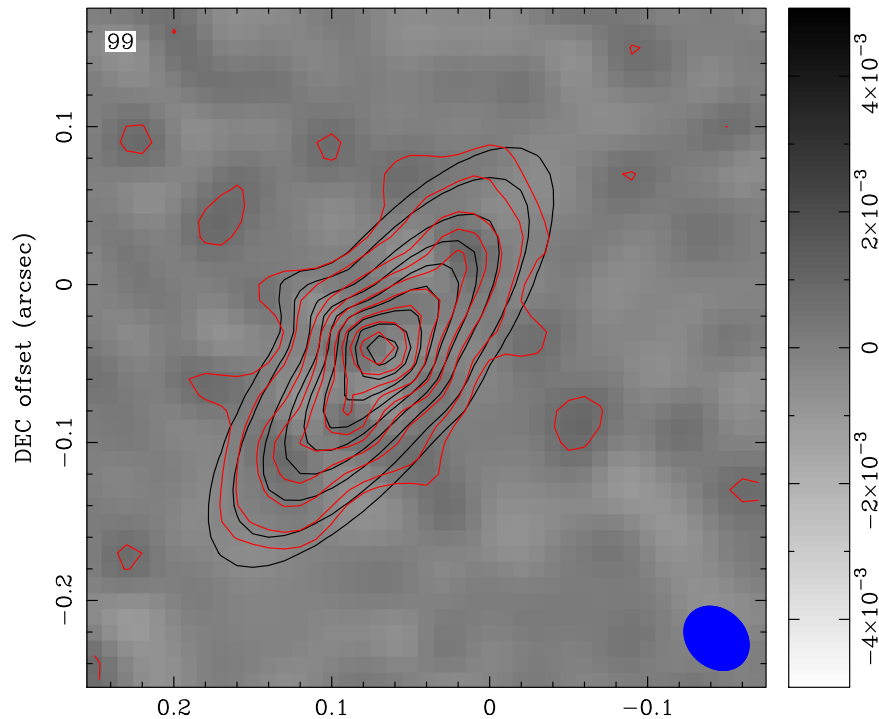
Figure 3. 99 GHz continuum emission and residuals to a two-Gaussian model fit. The red contours show the 99 GHz continuum emission at 56 × 42 mas resolution. The black contours show the two-Gaussian model, both with contours at 50, 100, 200, 300, 400, 500, 600, 700, 800, and 900 K. The pixel image shows residuals to the two-Gaussian model fit (units of jansky per beam). The synthesized beam FWHM is shown in the lower right.

data are not consistent with a compact jet, however the data do not preclude a more complex extended source with a weak compact component. The extended emission at 6 and 14 GHz favors a disk-wind hypothesis, in which both the molecular and ionized outflow are magneto-centrifugally driven from different regions in a rotationally supported disk (Blandford & Payne 1982; Matsushita et al. 2018). Vaidya & Goddi (2013) modeled an MHD disk wind from a high-mass protobinary, specifically tailored on Orion SrcI.

High-resolution observations at centimeter wavelengths are required to determine if SrcI harbors an ionized jet. Observations of Orion-KL obtained with the e-MERLIN telescope at 5 GHz (6 cm wavelength), in 2021, provided a synthesized beam FWHM 120 × 30 mas with 40% sidelobes, which resolved out large-scale structure. SrcI was not detected in images, both with or excluding short spacings ($uv < 200\,k\lambda$) to filter out large-scale structure. The upper limit on the SrcI brightness is 0.03 mJy beam^{-1} or 400 K (1σ). The intensity maximum around the position of SrcI is about 0.1 mJy beam^{-1} or ~1200 K at 3σ levels, which is consistent with the brightness temperature of the 43 GHz image. The nondetection of SrcI by e-MERLIN is not consistent with the Gaussian fit to the images from the JVLA in 2012 September 30 at 6 GHz with a synthesized beam 300 × 194 mas. Ionospheric wedges could spoil the e-MERLIN phase calibration, but the λ^2 dependence makes this unlikely at 5 GHz, and self-calibration on strong compact sources in the field of view around SrcI did not detect SrcI. Consistent results were obtained on the three e-MERLIN observation days. Twenty compact sources were detected in the field of view around SrcI at positions consistent with those measured by Forbrich et al. (2016). Some of these sources are resolved and attenuated in the e-MERLIN observations. The 5–6 GHz structure of SrcI may be resolved by the high sidelobe structure of the e-MERLIN synthesized beam, and/or be time variable. If the SrcI structure was significantly different from

the Gaussian fits, it could have been resolved below the detection level in the e-MERLIN observations. For example, if the SrcI structure has a north–south extent ~0″3 it is attenuated by a factor 10 by the 40% sidelobes in the e-MERLIN beam. High resolution with good uv coverage (e.g., ngVLA or SKA) will be needed to map the SrcI structure at centimeter wavelengths.

Recent radio continuum surveys have detected a number of high-mass young stellar objects (YSOs) associated with radio jets (Purser et al. 2016; Sanna et al. 2018). They are thought to be driven from the closer vicinity to the central YSOs given their higher velocities, of a few 100 km s^{-1}, than molecular outflows. In the MHD disk-wind model, a higher-velocity outflow is predicted to be launched in the rotating disk with a larger rotation velocity than the molecular outflow (Matsushita et al. 2018). Vaidya & Goddi (2013) found a lower MHD wind velocity for the protobinary disk model for Orion SrcI.

3.2. Spectral Energy Distribution

The SED of SrcI from 4 to 340 GHz is shown in Figure 4. To search for evidence of time variability in the SrcI fluxes, we have color-coded the data by year of observation. It does appear possible that SrcI has brightened somewhat over the 30 yr period spanned by these measurements, although much of the scatter in the data probably is due to the difficulty in measuring the flux of a compact source that is embedded in a complex, lumpy, extended medium.

At frequencies >43 GHz, the SED appears to follow a ν^2 curve, consistent with optically thick emission from dust in the SrcI disk. At lower frequencies, however, most of the flux densities—including the 6 and 14 GHz measurements reported in this paper—lie above this curve. Our images at 6 and 14 GHz show an extended region with SI < 2 along the minor
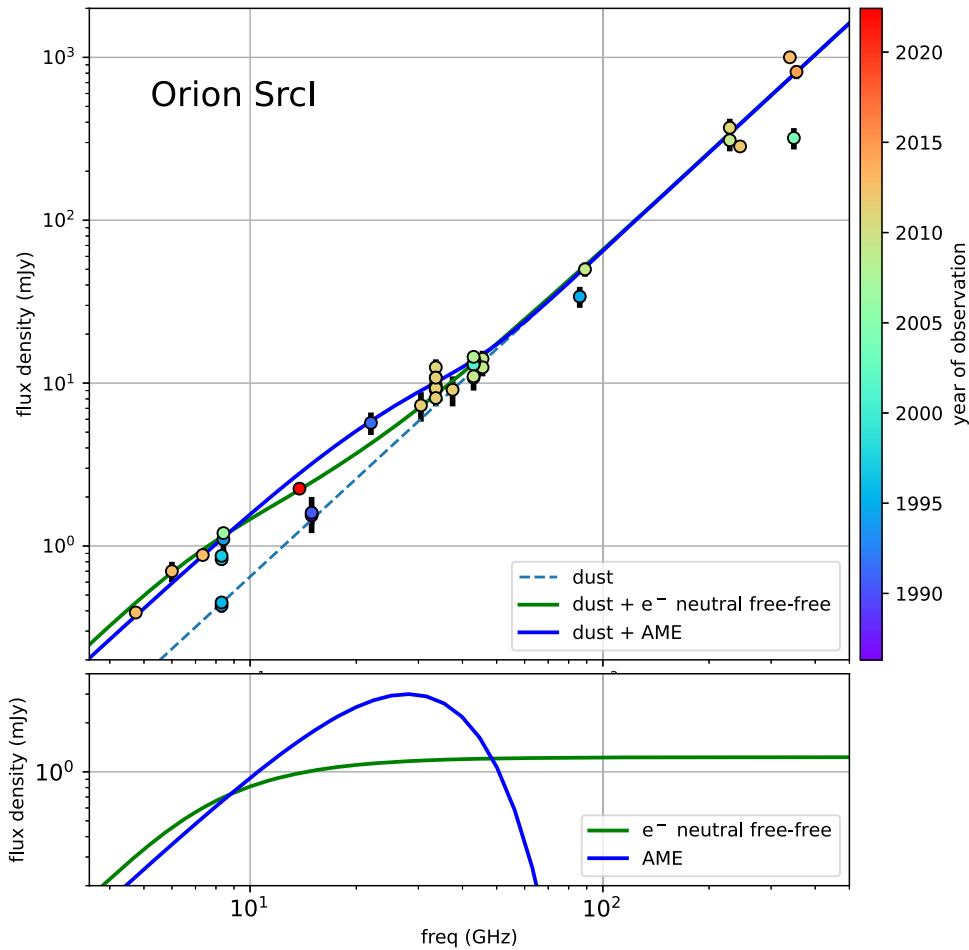
Figure 4. Spectral energy distribution of SrcI from centimeter to submillimeter wavelengths. References are given in Plambeck & Wright (2016). From ~43 to 350 GHz the data follow a ν^2 curve (dashed green line) that is fit to a flux density of 330 mJy at 229 GHz. At lower frequencies H-minus free–free emission (green curve), and anomalous microwave emission from spinning dust (blue curve) may become important. The observations are color-coded by year of observation. There is some evidence that flux densities have increased slightly since the 1990s. The published error bars for most of the flux measurements are smaller than the plot symbols.

axis. Wright et al. (2022) discuss mechanisms which could produce an SI < 2. Emission along the minor axis of the disk could arise from a separate emission mechanism. We consider several possible mechanisms in the sections below. Example curves for two of these, electron–neutral free–free emission and dipole radiation from spinning dust (anomalous microwave emission, AME), are shown in the lower panel of Figure 4.

3.2.1. Thermal Dust Emission

We first consider the possibility that the "excess" flux at low frequencies is thermal emission from hot dust close to the central object. This dust would emit at all frequencies, of course, but at millimeter wavelengths the emission might be absorbed by an extended envelope of cooler foreground dust. The Gaussian fit to the 6 GHz image indicates that the measured flux density of 0.7 mJy originates from an $0.''14 \times 0.''09$ region. This implies a 6 GHz brightness temperature of 3000 K, higher than the sublimation temperature of dust. However, radiation pressure from the protostars may shock and expel dusty material along the minor axis of the disk (Hosokawa & Omukai 2009). The wide-angle outflow observed in SiO emission shows that material is being ablated from the disk. Emission at centimeter wavelengths would require a population of pebble-sized grains in this outflow, which seems unlikely.

3.2.2. Ionized Outflow

An ionized outflow could have a spectral index < 2. The bulge to the northeast along the minor axis at 43 GHz and a smaller one at 99 GHz have a spectral index ~ 1. The Gaussian fits at 6, 14, 43, and 99 GHz show a component along the disk minor axis whose flux and length vary with frequency consistent with an ionized outflow from 6 to 99 GHz. Figure 5 plots the flux density and length (FWHM) of Gaussian fits along the minor axis of the 6, 14, 43, and 99 GHz continuum emission.

The total flux in the minor-axis component scales with frequency as $\nu^{0.5\pm0.1}$ from 6 to 99 GHz. The spectral index between 6 and 14 GHz steepens to 1.35 ± 0.1. At 6 GHz, Forbrich et al. (2016) derived a spectral index 1.86 ± 0.26 from the two 1 GHz basebands centered at 4.736 and 7.336 GHz. The steeper spectral index at lower frequency is consistent with the free–free emission fitted to the integrated flux measurements shown in Plambeck & Wright (2016, their Figure 14). The length of the minor-axis component decreases with frequency as $\nu^{-0.2\pm0.1}$ between 6 and 99 GHz. This is consistent with the ionized outflows discussed by Reynolds (1986), who show that a collimated ionized outflow can exhibit a wide range of parameters with spectral index from -0.1 to 2, varying along the outflow depending on the velocity gradients and confinement (see Reynolds 1986, their Figure 2), and note that variations in
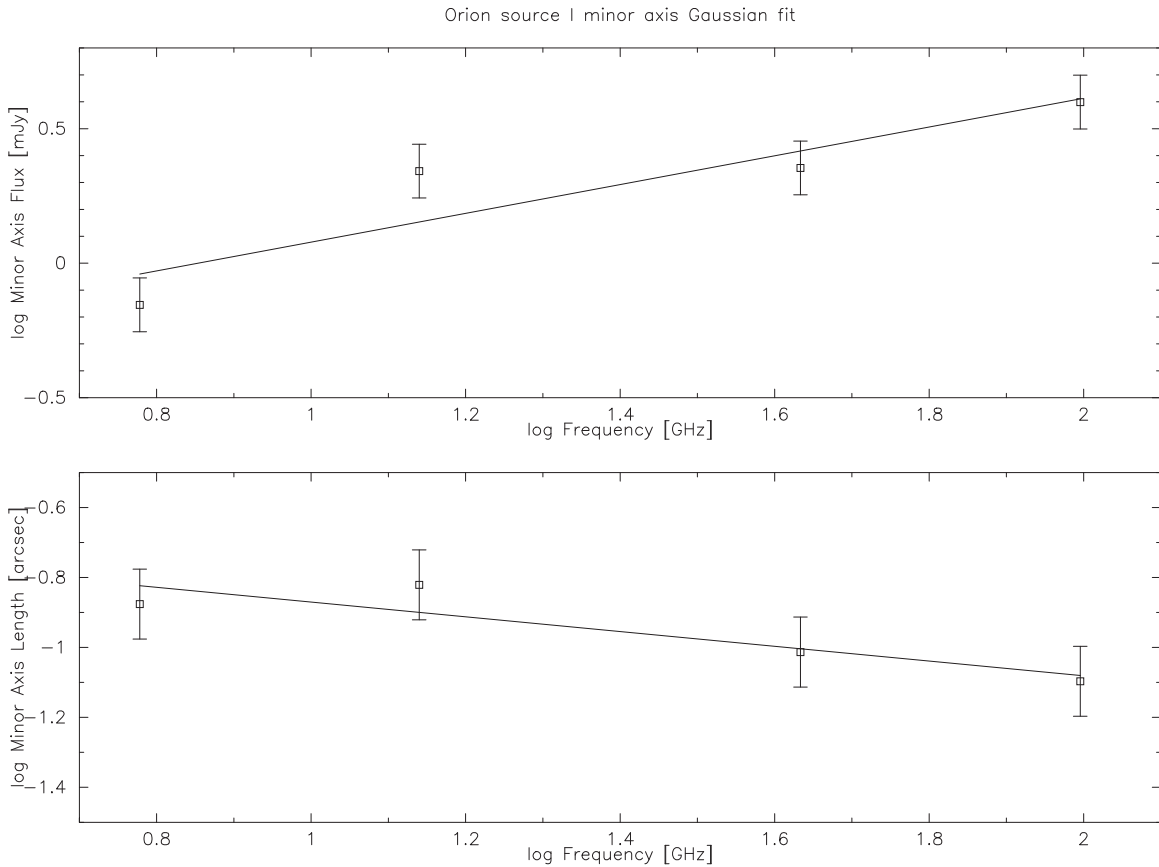
Figure 5. Flux density and length (FWHM) of Gaussian fits along the minor axis of the 6, 14, 43, and 99 GHz continuum emission. Least-squares fits are indicated by the straight black lines.

the flow along the outflow may yield observable spectral features. The residuals in Figure 2 presented here may represent such spectral variations along the outflow.

3.2.3. Free–Free Emission

The best evidence for free–free emission would be the detection of hydrogen recombination lines. These radio recombination lines (RRLs) will be visible only at frequencies greater than the turnover frequency where the continuum emission becomes optically thin. We have only upper limits on recombination lines. The ratio of the RRL to continuum intensity expected from pure free–free emission is ~1–2 at centimeter wavelengths (Gordon & Sorochenko 2002), so an upper limit on the RRLs would directly limit the free–free contribution to the continuum where any free–free component is optically thin. The line/continuum ratio increases with frequency so we looked for recombination lines at millimeter wavelengths. Assuming the outflow is corotating with the molecular outflow observed in SiO, we estimate a FWHM line width ~30 km s^{-1}. According to Equation 14.29 in Wilson et al. (2009), we find a line/continuum ratio of about 4 at 230 GHz. Plambeck & Wright (2016) analyzed the continuum flux densities measured for SrcI from 4 to 690 GHz. Free–free emission may become important where the dust emission becomes optically thin. Plambeck & Wright (2016, their Figure 14) show fits for a spectral index of 2, with excess emission at submillimeter wavelengths from dust emission, and free–free emission which fits the excess flux at centimeter wavelengths. The H26α (353.6 GHz) and H21α (662.4 GHz) hydrogen

recombination lines were not detected. Plambeck & Wright (2016) used a velocity range $5 < v_{\text{lsr}} < 23$ km s^{-1} to establish upper limits on the intensities of the recombination lines. No recombination lines were detected in the SrcI disk with an upper limit 5% of the total continuum flux integrated in a $0\overset{''}{.}2 \times 0\overset{''}{.}2$ box centered on SrcI.

We reexamined our observations of the H30α line at 231.9 GHz. We made spectral line images with 65 × 35 mas and 5 km s^{-1} resolution. The H30α recombination line was not detected in a velocity range −50 to +50 km s^{-1}. The peak brightness (±3σ) was 6 K, only 4% of the disk continuum brightness of 440 K. The ionization may be very different where the disk is exposed to radiation from the protostars or shocks generated in the outflow (Shull & McKee 1979), so an overall ionization fraction may not represent conditions in different parts of the disk. These observations do not exclude ionized emission at the 4% level in the disk, and 25% in the lower brightness bulge to the northwest, observed at 43 GHz. There may be substantial extinction by cooler dust that would obscure recombination lines, even along the minor axis of the disk. Báez-Rubio et al. (2018) modeled SrcI as dust and H-minus emission (see below). Their model in their Tables 3 and 4 show that dust opacity reduces the RRL detectability, rendering this diagnostic for ionization fraction less definitive.

Plambeck & Wright (2016, their Figure 14) plot a fit to the low-frequency integrated fluxes with a free–free component with $n_e = 5 \times 10^{-6}$ cm^{-3}. Using the fitted size of the observed emission at 6 to 43 GHz, we obtain a mass ~8 × 10^{-8} $M_\odot$ for electron–proton free–free emission.

The outflow in Figure 7 appears to expand and dissipate close to where the SiO $J = 1-0$ and $2-1$ ouflows mushroom out from a corotating SiO column (see Hirota et al. 2020, their Figure 2). Since the SiO outflow is rotating and expanding, an ionized outflow may also be rotating, and would expand and dissipate where the rotation velocity is similar to the velocity of SrcI through the ambient gas. Our H30α observations with 5 km s^{-1} resolution over 100 km s^{-1} would detect a rotating outflow, but a larger line width may be below the detection threshold. The RRL lines may have very broad line widths as, for example, in Cep A IRS1 (Jimenez-Serra et al. 2011). If the jet is highly turbulent or has a large opening angle the line width could be a few hundred km s^{-1}. Using Equation (24) in Anglada et al. (2018), the line-to-continuum ratio is $\sim$0.01 for a line width $\sim$200 km s^{-1}, and would not be detected in these observations.

3.2.4. Electron–Neutral Free–Free Emission

Electron–neutral free–free emission (Reid et al. 2007; Plambeck & Wright 2016) may be responsible for the higher flux densities in the SrcI disk below 43 GHz. Electron–neutral free–free (H-minus) emission occurs for temperatures between 1000 and 4500 K, where Na and K would be collisionally ionized but H and H$_2$ are neutral, and may be relevant in an ionized outflow from SrcI. Hirota et al. (2015) derived a spectral index 1.60 ± 0.24 for a combination of dust and H-minus emission to explain the emission from the SrcI disk for a range of total hydrogen densities from 10^{11} to 10^{14} cm^{-3} and temperatures 1200–3000 K. Báez-Rubio et al. (2018) modeled SrcI as dust and H-minus emission, assuming a cylindrical geometry for a neutral disk with dust, and derived a hydrogen density $0.5–7 \times 10^{11}$ cm^{-3}, with temperatures $\sim$1700 K at a radius 20 au estimated from 43 GHz images. Higher-resolution and higher-frequency data suggest optically thick dust as the opacity source in the SrcI disk (Hirota et al. 2016; Plambeck & Wright 2016). Although H-minus emission does not fit the overall spectral index of the disk where the emission is dominated by optically thick dust emission above $\sim$100 GHz, it might explain the observed SI for the emission along the minor axis, and in the outflow where our observations from 6 to 99 GHz show a component extended along the minor axis with an SI <2.

We calculated the H-minus free–free emission expected from gas in a $56 \times 36 \times 36$ au rectangular prism ($0''\!.14 \times 0''\!.09 \times 0''\!.09$) for a hydrogen density 4×10^{10} ($n[H2] = 2 \times 10^{10}$ cm^{-3}), and temperatures of 1500–1900 K. This is roughly the deconvolved FWHM sizes at 6 and 14 GHz, and would fit inside the boundary defined by SiO $v = 1$ and $v = 0$ masers. The total mass of gas in this prism is 0.008 $M_\odot$. If this material is flowing out from SrcI at 18 km s^{-1}, this implies a mass outflow rate of 10^{-3} $M_\odot$ yr^{-1}. The density and T_e are similar to those derived by Hirota et al. (2015) and Báez-Rubio et al. (2018), which assume different geometries, but an outflow 10^{-3} $M_\odot$ yr^{-1} is $\sim$100$\times$ that estimated from SiO, and would deplete the disk mass unless the accretion rate is also high (Wright et al. 2022). Figure 4 shows the excess low-frequency emission that could result from H-minus free–free emission in the total flux SED for SrcI. In this simple model, $n_e \sim 10^4$ cm^{-3}, and the fractional ionization $\sim$10^{-7} which may be too low to support an MHD outflow. Of course, the ionization might be higher where the disk is exposed to the protostars and shocks.

For regular free–free emission, the radiation arises from "collision" between H$^+$ (protons) and electrons, and each such collision provides an opportunity for the H$^+$ and electron to recombine. By contrast, for H-minus free–free emission, the radiation originates from collisions between neutral H and electrons. The exceedingly rare collisions between Na$^+$ and e$^-$ can result in recombination. The salt line at 232.51 GHz, which traces the rotation of the disk and correlates with the dust emission at the ends of the disk (Ginsburg et al. 2019), has emission at $v_{lsr} = 5$ km s^{-1} along the minor axis where it is exposed to ionizing radiation from the center of the disk. Na$^+$ RRLs, but not hydrogen recombination lines, would strongly suggest H-minus emission. As discussed by Ginsburg et al. (2019), the lowest excited electronic energy levels for NaCl is about 5 eV above the ground state, close to the photodissociation threshold (Zeiri & Balint-Kurti 1983; Silver et al. 1986), which may be dissociated by UV photons. UV emission may be produced in shocks in the outflow, and $\sim$5 eV photons could be produced by the central $\sim$4000 K photosphere (Testi et al. 2010) and ionize NaCl along the minor axis of the disk where the opacity is low. Báez-Rubio et al.'s (2018) models predict the expected RRL intensities in Na26α and K26α (see their Tables 3 and 4), which are below their observation rms limits of $\sim$49 and 20 mJy, respectively.

3.3. Alternatives to an Ionised Outflow

The lower spectral index along the minor axis of the SrcI disk and the bulge to the northwest at 43 GHz might also be explained by different conditions along the rotation axis of the disk. The wide-angle outflow observed in SiO emission shows that material is being ablated from the disk. Radiation pressure from the protostars may shock and expel dusty material along the minor axis of the disk (Hosokawa & Omukai 2009). We estimated radiation pressure at radius R, where $T = 1700$ and 500 K, as nominal inner and outer disk surface defined by the observations. For a spherical geometry and a central luminocity 10^4 $L_\odot$, we obtain inner and outer radii $R \sim 5.5$ au and 63 au. A disk geometry with surface $2\pi R^2(1 + d/R)$ with $d/R = 0.1$ gives similar R values. Equating the radiation and gas pressures, assuming that the gas has high opacity and dust is mixed with the gas, we estimate a velocity dispersion, v, for H$_2$, and density for pressure balance. For the inner surface $T \sim 1700$ K and $R \sim 5$ au, $v \sim 4$ km s^{-1} and N[H2] $\sim 10^{11}$ cm^{-3}. For the outer surface, $T \sim 500$ K and $R \sim 50$ au, $v \sim 2$ km s^{-1}, and N[H2] $\sim 7 \times 10^8$ cm^{-3}. This suggests that densities less than the above could be ablated and pushed away by radiation pressure. The bulge observed at 43 GHz could be partially ionized material ablated from the disk. Higher temperatures would strip off the grain mantles, releasing H$_2$O and other molecules with peak emission close to the disk (Wright et al. 2020).

The distribution of SiO, H$_2$O, and AlO emission provides additional chemical tracers of the outflow from SrcI. Figure 6 shows that the molecular outflow from the disk, mapped here in SiO $v = 0$, $J = 5-4$ emission at 5 km s^{-1} resolution, extends across the outflow seen in the 43 GHz continuum emission. We mapped the H$_2$O emission at 232.687 GHz, AlO $N = 6-5$ line at 229.69387 GHz, and the AlO $N = 9-8$ line at 344.4537 GHz (Wright et al. 2020). Figure 7 shows 229.694 GHz AlO emission overlaid on 43 GHz continuum and H$_2$O emission at 232.687 GHz. H$_2$O, AlO, and SiO maser emission are located along the sides of the outflow mapped at 43 GHz. AlO emission peaks are further out than H$_2$O, and are much brighter on the northeast side of SrcI where the outflow at 43 GHz is seen and the hot spot in the disk is located. The distributions of
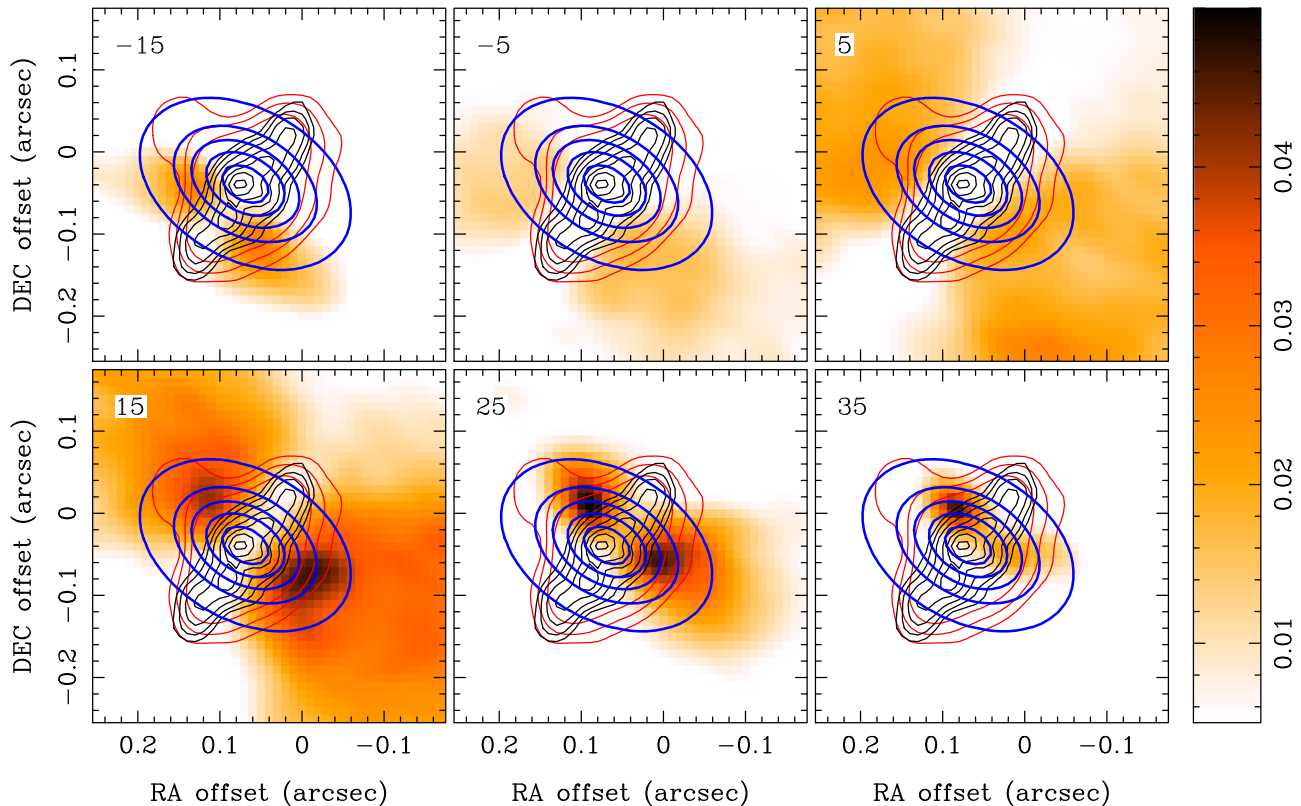
Figure 6. SiO $v = 0$ $J = 5-4$ emission at 217.10498 GHz overlaid on contours of the 99, 43, and 6 GHz continuum emission. The thick black contours at 99 GHz at 50, 100, 200, 300, 400, 500, 600, 700, 800, 900, and 1000 K with a 30 mas FWHM show the inner structure in the disk. The blue contours show the deconvolved Gaussian fit to the 6 GHz image. Contours at 100, 500, 900, 1300, 1700 K. The red contours at 43 GHz at 25, 50, and 100 K are convolved to 56×42 mas FWHM resolution to show the structure at the edge of the disk. The color image shows SiO $v = 0$, $J = 5-4$ emission at 10 km s^{-1} intervals (units of jansky per beam). Beam FWHM 54×34 mas with a PA 65°.

AlO emission and H_2O shown here are consistent with those for AlO $N = 13-12$ and $N = 17-16$ emission lines at 497 and 650 GHz (Tachibana et al. 2019), and H_2O at 463 GHz (Hirota et al. 2017). Tachibana et al. (2019) suggest that the AlO is produced at the base of the outflow and condenses further out into the outflow. Our observations with $\sim 4\times$ higher angular resolution show that AlO emission peaks downstream of the H_2O, and can be traced back to the ridge of continuum emission shown in Figure 7 at 99 GHz. AlO may be produced by grain destruction and oxidation by oxygen released by the dissociation of H_2O, or released as AlO further out in the outflow than the H_2O emission (Wright et al. 2020). These observations strongly suggest that the outflow is closely associated with grain chemistry in the outflow.

3.3.1. Anomalous Microwave Emission

The excess emission below ~ 100 GHz could also be caused by AME, which would lower the SI along the minor axis and in the outflow. Rafikov (2006) shows that AME from small spinning dust grains at $\nu < 50$ GHz can exceed thermal dust emission by a factor of several if more than $\sim 5\%$ of the carbon is in nanoparticles. Large grains are shattered by grain collisions in shocks. Jones et al. (1996) shows that for shock velocities 50–200 km s^{-1}, 5%–15% of grains $> 0.5\ \mu$m can be shattered into $\sim 0.1\ \mu$m fragments on timescales less than 10^8 yr in the warm medium. Nanograin production from larger grains is also predicted to occur close to sources of intense radiation by rotational disruption of dust grains by radiative torques (Hoang et al. 2019; Hoang 2021) and in shocks (Tram & Hoang 2019).

The formation of water ice mantles can affect the capacity of nanosilicates to generate AME (Mariñoso Guiu et al. 2021). Destruction of dust grains seems likely in the outflow to release H_2O, SiO, and AlO. Although dust grain mantles may not survive in the $\sim 500+$ K disk, fresh infalling material could bring in grains with mantles. Figure 4 shows the excess low-frequency emission that could result from AME from spinning dust grains in the total flux SED for SrcI. The AME flux may be time variable depending on the excitation of the spinning dust. If the spinning dust emission depends on time-variable shocks and radiation, it too may be variable.

3.3.2. Nonthermal Emission

The Very Long Baseline Array (VLBA) survey of the Orion region at 7 GHz (Forbrich et al. 2021) did not detect SrcI at four epochs between 2015 October 26 and 2018 October 26. The synthesized beam FWHM ranged from 4.7×1.6 mas to 2.8×1.2 mas with a shortest uv spacing ~ 3Mλ, corresponding to a largest angular size ~ 100 mas. The small synthesized beam and high-brightness temperatures in the VLBA observations require nonthermal emission (Forbrich et al. 2021). The VLBA observations set a 5.5σ upper limit of 0.21 mJy for SrcI structure smaller than ~ 100 mas. For optically thick emission, this may be resolved out entirely without any information on nonthermal emission.

3.3.3. Episodic Emission

Many of the other sources in the FOV are variable in these VLBA observations. Variable emission at 5–7 GHz could be
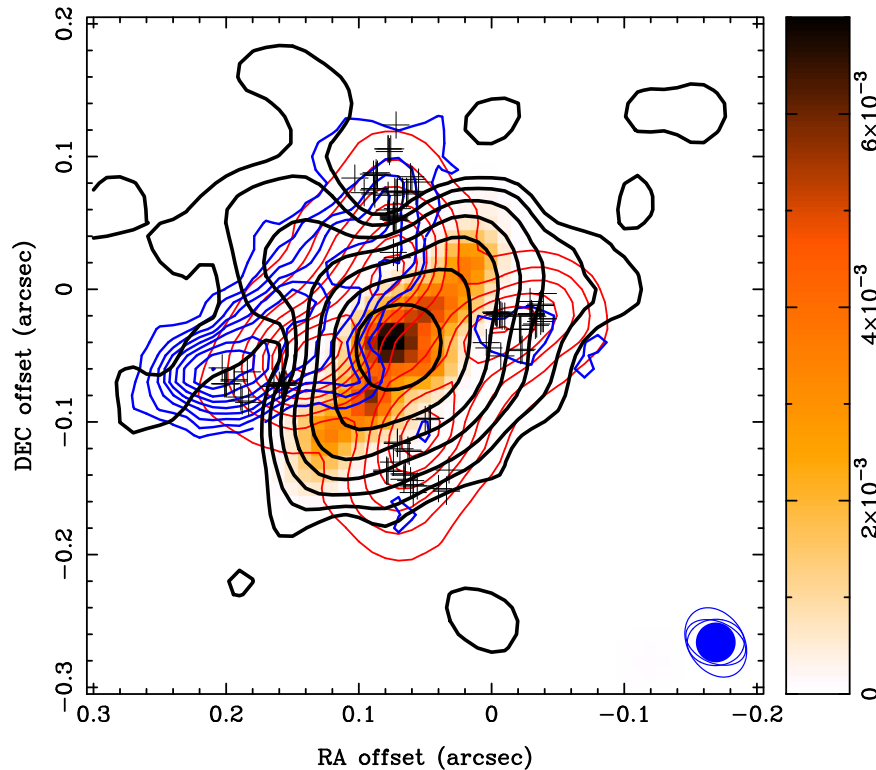
Figure 7. AlO, H_2O, and SiO maser emission, overlaid on contours of the 43 GHz and 99 GHz continuum emission. The black contours at 8, 16, 32, 64, 128, 256, and 512 K show the low-brightness emission at the edge of the disk at 43 GHz. The black crosses indicate the centroid positions of the $v = 1$, $J = 2-1$ SiO masers mapped by Issaoun et al. (2017). Red contours show the H_2O emission at 232.6867 GHz integrated over a velocity range $(-50$ to $50)$ km s^{-1}. Lowest contour 3000, contour interval 2000 K km s^{-1}. Blue contours show the AlO $N = 6-5$ emission integrated over -50 to 50 km s^{-1}. Lowest contour 500, contour interval 500 K km s^{-1}. The 30 mas convolving beam FWHM for the 99 GHz continuum color image (units of jansky per beam) is indicated with a blue filled circle. The convolving beam at 43 GHz, 56×42 mas FWHM resolution, is shown in the lower right. The FWHM beams for the H_2O emission of $0\rlap{.}''05 \times 0\rlap{.}''03$ with a PA 65°, and for the AlO $N = 6-5$, $0\rlap{.}''04 \times 0\rlap{.}''03$ with a PA $-88°$, are also shown as the open ellipses in the lower right.

associated with episodic accretion events onto the embedded protostars with structural or excitation changes in the ionized or nonthermal emission.

A possible reason for nondetection by e-MERLIN is an increase in size from $0\rlap{.}''1$ to $\sim 0\rlap{.}''5$ in the ~ 9 yr between the JVLA and e-MERLIN observations, which would correspond to a velocity ~ 80 km s^{-1} in the plane of the sky.

Other massive young protostars have radio jets with high proper motions. In Cepheus A, the radio jet has a proper motion ~ 500 km s^{-1} (Curiel et al. 2006). Cunningham et al. (2009) proposed that the precessing jet is driven by the massive protostellar source HW2, with close passages of a companion in an eccentric orbit, which perturbs the disk and triggers accretion and episodes of jet production.

In the high-mass protobinary system IRAS 165474247 the ionized jet appears to come from only one of the binary protostars (Tanaka et al. 2020). Such a jet might be associated with episodic or periodic accretion corresponding to the orbital period of the binary.

Similar to these high-mass YSOs (Purser et al. 2016, Sanna et al. 2018), there could be a compact radio jet in SrcI emanating from the inner region. Considering the large specific angular momentum carried by the molecular outflow, it is unlikely that a radio jet in SrcI could entrain the outflow traced by the Si^{18}O line (Hirota et al. 2017). If higher-resolution observations do not identify a radio jet driven from SrcI, this would also suggest that the molecular outflow in SrcI is not driven by an entrainment in a jet.

For Orion SrcI, with a binary separation 1–9 au suggested by the BN/SrcI explosion (Goddi et al. 2011b), the orbital period would equal ~ 0.3–10 yr. The outflow and ionization of the

material along the minor axis in SrcI might be expected to echo accretion flows, leading to the intriguing possibility of mapping accretion events, and determining the orbital parameters of compact binary systems like Orion SrcI, from time variations in the centimeter-wavelength emission.

4. Summary

1. We present images at 6 and 14 GHz of emission from SrcI in Orion-KL with $\sim 0\rlap{.}''3 \times 0\rlap{.}''2$ resolution. The 6 and 14 GHz emission trace structure along the minor axis of the disk also apparent in images from 43 to 340 GHz.

2. Although the high opacity at 220–340 GHz hides the internal structure, images at 43–99 GHz reveal structure within the disk. Images of the spectral index distributions show an extensive region with spectral index <2 along the minor axis.

3. Gaussian fits at 6, 14, 43, and 99 GHz show a component along the disk minor axis whose flux and length vary with frequency, consistent with an ionized outflow.

4. The 43 GHz images from 2002 to 2009 (Goddi et al. 2011b) are consistent with this component along the minor axis of the disk within $\sim 10\%$. There is no significant change in the morphology or PA of the structure at 43 GHz over 8 yr.

5. SrcI was undetected in higher-angular-resolution e-MERLIN observations at 5 GHz in 2021. The 5–6 GHz structure of SrcI may be resolved out by the high sidelobe structure of the e-MERLIN synthesized beam, or be time variable. If the SrcI structure was significantly different from

the Gaussian fit, it could have been resolved below the detection level in the e-MERLIN observations.

6. The extended emission at 6 and 14 GHz favors a disk-wind hypothesis, in which both the molecular and ionized outflow are magneto-centrifugally driven in a rotationally supported disk.

7. The correlation with SiO masers, H2O, and AlO suggests that the 6–99 GHz extension along the minor axis is associated with dust grain destruction, and a dusty, partially ionized outflow of material pushed out from the disk by the luminosity of the star(s).

8. Future high-resolution and well-calibrated observations at centimeter wavelengths will help to distinguish between the different emission mechanisms, and look for time variations in the structure of the disk and outflow.

Facilities: ALMA, VLA, e-MERLIN.

Software: Miriad (Sault et al. 1995).

ORCID iDs

Melvyn Wright ⓘ https://orcid.org/0000-0002-9154-2440
Tomoya Hirota ⓘ https://orcid.org/0000-0003-1659-095X
Jan Forbrich ⓘ https://orcid.org/0000-0001-8694-4966
Richard Plambeck ⓘ https://orcid.org/0000-0001-6765-9609
John Bally ⓘ https://orcid.org/0000-0001-8135-6612
Ciriaco Goddi ⓘ https://orcid.org/0000-0002-2542-7743
Adam Ginsburg ⓘ https://orcid.org/0000-0001-6431-9633
Brett McGuire ⓘ https://orcid.org/0000-0003-1254-4817

References

Anglada, G., Rodríguez, L. F., & Carrasco-González, C. 2018, A&ARv, 26, 3
Báez-Rubio, A., Jiménez-Serra, I., Martín-Pintado, J., Zhang, Q., & Curiel, S. 2018, ApJ, 853, 4
Bally, J., Ginsburg, A., Forbrich, J., & Vargas-González, J. 2020, ApJ, 889, 178
Blandford, R. D., & Payne, D. G. 1982, MNRAS, 199, 883
Commerçon, B., González, M., Mignon-Risse, R., Hennebelle, P., & Vaytet, N. 2022, A&A, 658, A52
Cunningham, N. J., Moeckel, N., & Bally, J. 2009, ApJ, 692, 943
Curiel, S., Ho, P. T. P., Patel, N. A., et al. 2006, ApJ, 638, 878
Forbrich, J., Dzib, S. A., Reid, M. J., & Menten, K. M. 2021, ApJ, 906, 23
Forbrich, J., Rivilla, V. M., Menten, K. M., et al. 2016, ApJ, 822, 93
Ginsburg, A., Bally, J., Goddi, C., Plambeck, R., & Wright, M. 2018, ApJ, 860, 119
Ginsburg, A., McGuire, B., Plambeck, R., et al. 2019, ApJ, 872, 54
Goddi, C., Greenhill, L. J., Chandler, C. J., et al. 2009, ApJ, 698, 1165
Goddi, C., Greenhill, L. J., Humphreys, E. M. L., Chandler, C. J., & Matthews, L. D. 2011a, ApJL, 739, L13
Goddi, C., Humphreys, E. M. L., Greenhill, L. J., Chandler, C. J., & Matthews, L. D. 2011b, ApJ, 728, 15
Gómez, L., Rodríguez, L. F., Loinard, L., et al. 2008, ApJ, 685, 333
Gordon, M. A., & Sorochenko, R. L. 2002, Radio Recombination Lines. Their Physics and Astronomical Applications, Vol. 282 (Dordrecht: Kluwer)
Greenhill, L. J., Goddi, C., Chandler, C. J., Matthews, L. D., & Humphreys, E. M. L. 2013, ApJL, 770, L32
Hirota, T., Kim, M. K., & Honma, M. 2016, ApJ, 817, 168
Hirota, T., Kim, M. K., Kurono, Y., & Honma, M. 2014, ApJL, 782, L28
Hirota, T., Kim, M. K., Kurono, Y., & Honma, M. 2015, ApJ, 801, 82
Hirota, T., Machida, M. N., Matsushita, Y., et al. 2017, NatAs, 1, 0146
Hirota, T., Plambeck, R. L., Wright, M. C. H., et al. 2020, ApJ, 896, 157
Hoang, T. 2021, ApJ, 921, 21
Hoang, T., Tram, L. N., Lee, H., & Ahn, S.-H. 2019, NatAs, 3, 766
Hosokawa, T., & Omukai, K. 2009, ApJ, 691, 823
Issaoun, S., Goddi, C., Matthews, L. D., et al. 2017, A&A, 606, A126
Jimenez-Serra, I., Martín-Pintado, J., Baez-Rubio, A., Patel, N., & Thum, C. 2011, ApJL, 732, L27
Jones, A. P., Tielens, A. G. G. M., & Hollenbach, D. J. 1996, ApJ, 469, 740
Kim, M. K., Hirota, T., Honma, M., et al. 2008, PASJ, 60, 991
Kounkel, M., Covey, K., Suárez, G., et al. 2018, AJ, 156, 84
Mariñoso Guiu, J., Ferrero, S., Macià Escatllar, A., Rimola, A., & Bromley, S. T. 2021, FrASS, 8, 80
Matsushita, Y., Sakurai, Y., Hosokawa, T., & Machida, M. N. 2018, MNRAS, 475, 391
Matthews, L. D., Greenhill, L. J., Goddi, C., et al. 2010, ApJ, 708, 80
Menten, K. M., Reid, M. J., Forbrich, J., & Brunthaler, A. 2007, A&A, 474, 515
Niederhofer, F., Humphreys, E. M. L., & Goddi, C. 2012, A&A, 548, A69
Plambeck, R. L., & Wright, M. C. H. 2016, ApJ, 833, 219
Plambeck, R. L., Wright, M. C. H., Friedel, D. N., et al. 2009, ApJL, 704, L25
Purser, S. J. D., Lumsden, S. L., Hoare, M. G., et al. 2016, MNRAS, 460, 1039
Rafikov, R. R. 2006, ApJ, 646, 288
Reid, M. J., Menten, K. M., Greenhill, L. J., & Chandler, C. J. 2007, ApJ, 664, 950
Reynolds, S. P. 1986, ApJ, 304, 713
Rodríguez, L. F., Dzib, S. A., Loinard, L., et al. 2017, ApJ, 834, 140
Rodríguez, L. F., Dzib, S. A., Zapata, L., et al. 2020, ApJ, 892, 82
Rodríguez, L. F., Poveda, A., Lizano, S., & Allen, C. 2005, ApJL, 627, L65
Sanna, A., Moscadelli, L., Goddi, C., Krishnan, V., & Massi, F. 2018, A&A, 619, A107
Sault, R. J., Teuben, P. J., & Wright, M. C. H. 1995, in ASP Conf. Ser. 77, Astronomical Data Analysis Software and Systems IV, ed. R. A. Shaw, H. E. Payne, & J. J. E. Hayes (San Francisco, CA: ASP), 433
Shull, J. M., & McKee, C. F. 1979, ApJ, 227, 131
Silver, J. A., Worsnop, D. R., Freedman, A., & Kolb, C. E. 1986, JChPh, 84, 4378
Tachibana, S., Kamizuka, T., Hirota, T., et al. 2019, ApJL, 875, L29
Tanaka, K. E. I., Zhang, Y., Hirota, T., et al. 2020, ApJL, 900, L2
Testi, L., Tan, J. C., & Palla, F. 2010, A&A, 522, A44
Tram, L. N., & Hoang, T. 2019, ApJ, 886, 44
Vaidya, B., & Goddi, C. 2013, MNRAS, 429, L50
Wilson, T. L., Rohlfs, K., & Hüttemeister, S. 2009, Tools of Radio Astronomy (Berlin: Springer)
Wright, M., Bally, J., Hirota, T., et al. 2022, ApJ, 924, 107
Wright, M., Plambeck, R., Hirota, T., et al. 2020, ApJ, 889, 155
Zeiri, Y., & Balint-Kurti, G. G. 1983, JMoSp, 99, 1